# Frequency domain modelling of transversely isotropic viscoelastic fibre-reinforced plastics

**Wilfried V. Liebig, Alexander Jackstadt, Vincent Sessner, Kay A. Weidenmann, Luise Kärger**

**Angaben zur Veröffentlichung / Publication details:**

Liebig, Wilfried V., Alexander Jackstadt, Vincent Sessner, Kay A. Weidenmann, and Luise Kärger. 2019. "Frequency domain modelling of transversely isotropic viscoelastic fibre-reinforced plastics." *Composites Science and Technology* 180: 101–10. https://doi.org/10.1016/j.compscitech.2019.04.019.

# Frequency domain modelling of transversely isotropic viscoelastic fibre-reinforced plastics

Wilfried V. Liebig[a,*], Alexander Jackstadt[a], Vincent Sessner[b], Kay A. Weidenmann[b], Luise Kärger[a]

[a] Karlsruhe Institute of Technology, Institute of Vehicle System Technology, Lightweight Technology, Rintheimer Querallee 2, D-76131 Karlsruhe, Germany
[b] Karlsruhe Institute of Technology, Institute for Applied Materials, Hybrid and Lightweight Materials, Engelbert-Arnold-Strasse 4, D-76131 Karlsruhe, Germany

## 1. Introduction

The steady rise in fibre-reinforced plastics (FRP) being a material of choice for mechanical design solutions in various applications over the past decades is to a large part ascribable to their remarkable high stiffness and strength. At the same time FRP are of low density compared to conventional materials such as metals. While this offers a variety of opportunities in the design of lightweight structural components for aerospace, automotive, shipbuilding and energy applications, the time and strain rate dependency of those materials with polymeric matrices still poses a challenge to the engineer. On the one hand, viscoelastic creep and relaxation processes can be undesirable and need to be accounted for in the design and dimensioning phase of product development. On the other hand, viscoelastic materials also allow for material damping when subjected to dynamic loads without the necessity of additional structural damping elements. Fundamental work in the field of describing viscoelastic effects in terms of fibre-reinforced composites is done by Schapery [1], Hiel et al. [2] and Brinson and Knauss [3]. In any case, an adequate depiction of the viscoelastic material behaviour of FRP becomes necessary in order to apply those materials in structural components. Commonly referenced material models are published in Refs. [4–7].

Owing to the time- and cost-intensive identification of viscoelastic material parameters by means of relaxation respectively creep tests or DMA, numerical micromechanics have been proven a viable alternative in a number of recent publications [8–12]. The advantages of dynamic steady-state analyses on statistically representative volume elements (SRVE) have so far only been exploited by Pathan et al. [13,14] and found to be suitable for depicting the viscoelastic behaviour of FRP by Javid et al. [15]. However, only a limited frequency range is considered and no further elaboration is given on the implementation of the viscoelastic material models based on the homogenised data. Rösner et al. [9] use homogenisation techniques on an RVE to parametrise a nonlinear orthotropic viscoelastic material model. The model is only implemented in the time domain and the fact that merely a second order generalised Maxwell model (GMM) is considered forbids the transition to a wider frequency range.

In contrast to previous works, which focused mostly on creep and relaxation, in this work, a micro-scale approach considering the transverse isotropy and viscoelasticity of FRP under dynamic loads in the frequency domain is developed. This concept allows for the use of

* Corresponding author.
*E-mail addresses:* wilfried.liebig@kit.edu (W.V. Liebig), alexander.jackstadt@kit.edu (A. Jackstadt), vincent.sessner@kit.edu (V. Sessner), kay.weidenmann@kit.edu (K.A. Weidenmann), luise.kaerger@kit.edu (L. Kärger).

computationally efficient steady-state analyses as opposed to the resource demanding time-domain modelling of long lasting creep and relaxation tests. On the micro-scale (discrete modelling of individual fibres embedded in a matrix), an SRVE of a unidirectionally (UD) FRP under harmonic excitation is developed. Its frequency response can then be directly obtained via homogenisation by volume averaging over the SRVE [16] and thus the identification of material parameters describing the linear viscoelastic behaviour on the macro-scale. Furthermore, a user-defined material model (UMAT), for which a minimal working example can be found in the supplementary data, is developed and implemented for the use in frequency domain steady-state analyses in the commercial FEM software Abaqus®.

## 2. Numerical modelling approach

### 2.1. Statistically representative volume element

Numerical studies on the micro-scale are performed on an SRVE under periodic boundary conditions by using commercial FE software Abaqus®. An established algorithm for the creation of random fibre distributions for the use in SRVEs is developed by Melro et al. [17] and is implemented for this study. According to the approach from Melro et al. [17] the high fibre volume content for the random distribution of fibres is achieved in three steps: 1. Fibres are randomly placed within the volume; 2. Fibres are stirred to create matrix-rich areas where further fibres can be placed; 3. Compaction of fibres in the outskirts leads to further possibilities to place fibres. All steps include a compatibility check to avoid fibre overlapping.

Following model parameters refer to the coordinate system as defined in Fig. 1. The length $a_1 = 0.5\,\mu\text{m}$ of the SRVE in fibre direction has been chosen in order to accommodate only one row of elements. Among others, Melro et al. [18] concluded, that the model length in fibre direction does not influence the prediction accuracy for mechanical properties of FRPs. The mean fibre diameter ($d_\text{f} = 7\,\mu\text{m} \pm 0.3\,\mu\text{m}$) and its standard deviation are determined from a light microscopy image. Based on those, a Gaussian distribution for the fibre diameter is assumed and the SRVE is created accordingly as explained above. The cross section's dimensions $a_2 = a_3 = 87.5\,\mu\text{m}$ are chosen so that the aspect ratio $\delta = a_2/d_\text{f} = 12.5$ is respected. This is the minimum ratio identified by Pathan et al. [13] which is needed for accurate and statistically meaningful predictions of viscoelastic properties on SRVEs. Element types C3D20R and C3D15 with an approximate length of 0.5 µm are used, resulting in meshes containing approximately 40000 elements. The element size has been identified by a mesh fineness study. Fig. 2 shows SRVEs with different fibre volume contents $v_\text{f}$ of 30%, 40%, 52%, 56%, 60% and 69%, which are studied in the following.

In general, the SRVE is excited with a sinusoidal varying displacement of constant amplitude under steady-state conditions, so that an isostrain state in terms of strain amplitude is reached. The simulations are carried out by using a direct-solution steady-state dynamic analysis covering a frequency range of $10^{-6}$ Hz to $10^{6}$ Hz. Six load cases are considered, each leading to a single strain component becoming non-zero.

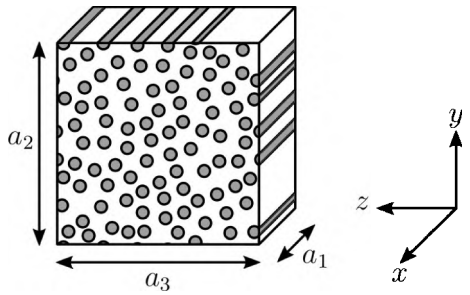


**Fig. 1.** Statistically representative volume element (SRVE) dimensions and its coordinate system.

In this study a UD FRP with the following mechanical characteristics of fibres and matrix is investigated. The carbon fibres are assumed to behave transversely isotropic and are modelled based on Torayca® T700S high strength carbon fibres by Toray Carbon Fibers America, Inc. The linear elastic material properties are listed in Table 1 and are based on the manufacturer's data sheet [19], namely the Young's modulus $E_\text{L}$. The remaining elastic constants ($E_\text{T}$, $\nu_\text{LT}$, $G_\text{LT}$ and $G_\text{TT}$) not listed in the data sheet are retrieved from Schürmann [20] for an equivalent carbon fibre, which has similar elastic properties. According to the manufacturer's data sheet, the fibre density is $\rho_\text{f} = 1.8\ \text{gcm}^{-3}$ [19]. The matrix is modelled as an isotropic linear viscoelastic material with the linear elastic properties summarised in Table 2, where the Young's modulus $E$, Poisson's ratio $\nu$ and density $\rho_\text{m}$ are provided by Hexcel [21]. Also provided by the manufacturer are dynamic mechanical data of the epoxy at a frequency $f = 1$ Hz between 20°C and 200°C. According to Martynenko and Lvov [10], the difference in temperature dependency between the reinforced composite (transverse loading direction) and the neat epoxy is negligible, so the procedure described in Sec. 3.2 is chosen to determine the dynamic viscoelastic properties of the matrix.

### 2.2. Deduction of the macroscopic viscoelastic material models

For linear elastic materials, the generalised Hooke's law describes the constitutive relation between stress $\boldsymbol{\sigma}$ and strain $\boldsymbol{\varepsilon}$

$$\boldsymbol{\sigma} = \mathbb{C}\boldsymbol{\varepsilon}. \tag{1}$$

Here, $\boldsymbol{\sigma}$ corresponds to the Cauchy stress tensor, $\boldsymbol{\varepsilon}$ to the infinitesimal strain tensor and $\mathbb{C}$ to the fourth-order stiffness tensor. In the following, Eq. (1) is represented in a contracted notation compliant with Abaqus/Standard Eqn

$$\begin{pmatrix}\sigma_{11}\\ \sigma_{22}\\ \sigma_{33}\\ \sigma_{12}\\ \sigma_{13}\\ \sigma_{23}\end{pmatrix} = \begin{bmatrix} C_{1111} & C_{1122} & C_{1122} & 0 & 0 & 0 \\ & C_{2222} & C_{2233} & 0 & 0 & 0 \\ & & C_{2222} & 0 & 0 & 0 \\ & & & C_{1212} & 0 & 0 \\ & \text{sym.} & & & C_{1212} & 0 \\ & & & & & \frac{1}{2}(C_{2222}-C_{2233}) \end{bmatrix} \begin{pmatrix}\varepsilon_{11}\\ \varepsilon_{22}\\ \varepsilon_{33}\\ 2\varepsilon_{12}\\ 2\varepsilon_{13}\\ 2\varepsilon_{23}\end{pmatrix}. \tag{2}$$

The stiffness tensor $\mathbb{C}$ has a maximum of 21 independent elastic constants for fully anisotropic materials. When considering a transversally isotropic material displaying an infinite number of symmetry planes all perpendicular to a single axis of symmetry, the number of independent material constants can be reduced to five. Transverse isotropy is particularly suitable when describing UD FRP with a random distribution of fibres.

A generalised three-dimensional expression of linear viscoelasticity in the frequency domain is obtained by replacing the stiffness tensor $\mathbb{C}$ with the complex form

$$\mathbb{C}^*(\omega) = \mathbb{C}'(\omega) + \mathrm{i}\mathbb{C}''(\omega), \tag{3}$$

consisting of a real part (storage modulus $C'(\omega)$) and an imaginary part (loss modulus $C''(\omega)$).

Here, ω is the circular frequency and corresponds to the frequency $f$ by $\omega = 2\pi f$. The storage modulus describes the elastic part of the material behaviour and is proportional to the elastic deformation energy which is stored in the loaded material and which can be fully recovered after unloading. In contrast to that, the loss modulus represents the viscous part and corresponds to the dissipative energy which is converted into heat by internal friction. A transversely isotropic constitutive relation is obtained accordingly. This procedure is compliant with the viscoelastic correspondence principle, introduced by Read [22], stating that an elastic solution can be transformed to a viscoelastic one by replacing all quantities in the constitutive relation with appropriate complex functions representing viscoelastic properties. In general, a three-dimensional representation is thereby given by

$$\boldsymbol{\sigma}^*(\omega) = \mathbb{C}^*(\omega)\boldsymbol{\varepsilon}^*(\omega). \tag{4}$$

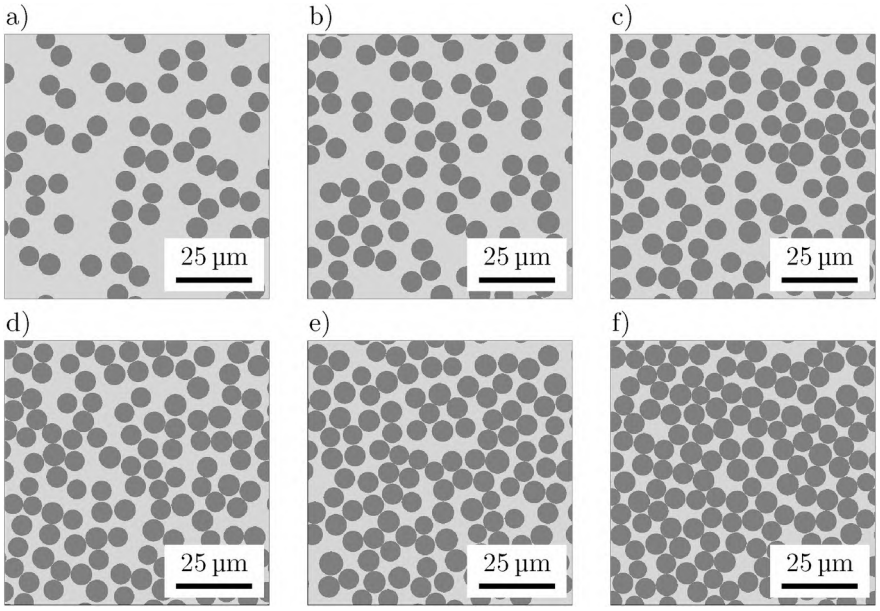


**Fig. 2.** Cross sections (dark gray coloured are fibres, light gray coloured is the matrix) of SRVEs with fibre volume content of a) $v_f = 30\%$, b) $v_f = 40\%$, c) $v_f = 52\%$, d) $v_f = 56\%$, e) $v_f = 60\%$ and f) $v_f = 69\%$.

**Table 1**
Elastic material properties of carbon fibre Torayca T700S.

| Young's moduli | | Poisson's ratio | Shear moduli | |
|---|---|---|---|---|
| $E_L$/GPa | $E_T$/GPa | $\nu_{LT}$/– | $G_{LT}$/GPa | $G_{TT}$/GPa |
| 230.0 | 28.0 | 0.23 | 50.0 | 16.7 |

**Table 2**
Material properties of epoxy matrix HexPly M77.

| Young's modulus | Poisson's ratio | Density |
|---|---|---|
| $E$/GPa | $\nu$/- | $\rho_m$/gcm$^{-3}$ |
| 3.41 | 0.41 | 1.15 |

Transversally isotropic material behaviour can be obtained by the introduction of five independent complex stiffness tensor components $C^*_{1111}$, $C^*_{2222}$, $C^*_{1122}$, $C^*_{2233}$ and $C^*_{1212}$. Commonly used engineering constants (namely two Young's moduli $E^*_L$ and $E^*_T$, one Poisson's ratio $\nu^*_{LT}$ and two shear moduli $G^*_{LT}$ and $G^*_{TT}$) can be directly derived from the aforementioned five independent complex stiffness tensor components. The subscript L relates to a quantity in longitudinal direction of the fibres, while the subscript T denotes a quantity in transverse direction, thus perpendicular to the fibre direction. The following equations show the relation between complex stiffness tensor components and the complex engineering constants:

$$E^*_L = C^*_{1111} - \frac{2C^{*2}_{1122}}{C^*_{2222} - C^*_{2233}} \tag{5}$$

$$E^*_T = \frac{C^*_{2222} - C^*_{2233}}{C^*_{1111}C^*_{2222} - C^{*2}_{1122}}(C^*_{1111}(C^*_{2222} + C^*_{2233}) - 2C^{*2}_{1122}) \tag{6}$$

$$\nu^*_{LT} = \frac{C^*_{1122}}{C^*_{2222} + C^*_{2233}} \tag{7}$$

$$G^*_{LT} = C^*_{1212} \tag{8}$$

$$G^*_{TT} = \frac{1}{2}(C^*_{2222} - C^*_{2233}). \tag{9}$$

*Generalised Maxwell model.* In order to describe the linear viscoelastic material behaviour investigated in this work, a generalised Maxwell model is chosen. The GMM can be classified as a rheological model thus consisting of a number of basic spring and dashpot elements. Every spring element with its stiffness $C_i$ stands for a linear elastic contribution to the material behaviour whereas every dashpot element with viscosity $\mu_i$ attributes to the linear viscous behaviour [23]. The GMM combines a number $N$ of Maxwell elements and a linear spring in parallel for the storage modulus

$$C'^{GMM}(\omega) = C_0\left(1 - \sum_{i=1}^{N} c_i\right) + C_0 \sum_{i=1}^{N} \frac{c_i \tau_i^2 \omega^2}{1 + \tau_i^2 \omega^2} \tag{10}$$

and the loss modulus

$$C''^{GMM}(\omega) = C_0 \sum_{i=1}^{N} \frac{c_i \tau_i \omega}{1 + \tau_i^2 \omega^2} \tag{11}$$

in the frequency domain.

In general, the storage modulus $C'$ and the loss modulus $C''$ can be defined as functions of the circular frequency ω, the elastic (instantaneous) modulus $C_0$, the normalised relaxation moduli $c_i = C_i/C_0$ and the relaxation time $\tau_i = \mu_i/C_i$ of every single Maxwell element $i$. The number $N$ of Maxwell elements is chosen depending on the number of observed decades as recommended by the Abaqus documentation [24]. Corresponding to that, $1 + 2N$ parameters must be determined per $C^*_{ijkl}$.

*Generalised fractional Maxwell model.* An extension of the well known GMM approach can be obtained by replacing the Maxwell elements from the GMM with "springpots", which is an interpolation between elastic (spring) and viscous (dashpot) behaviour. The resulting additional parameter α is a non-integer derivative and has to be $0 \leq \alpha \leq 1$. This leads to

$$C'^{GFMM}(\omega) = C_0\left(1 - \sum_{i=1}^{N} c_i\right) + C_0 \sum_{i=1}^{N} c_i \frac{(\omega\tau_i)^{2a_i} + (\omega\tau_i)^{a_i}\cos\frac{\pi a_i}{2}}{1 + (\omega\tau_i)^{2a_i} + 2(\omega\tau_i)^{a_i}\cos\frac{\pi a_i}{2}} \tag{12}$$

for the storage and

$$C''^{GFMM}(\omega) = C_0\left(1 - \sum_{i=1}^{N} c_i\right) + C_0 \sum_{i=1}^{N} c_i \frac{(\omega\tau_i)^{a_i}\sin\frac{\pi a_i}{2}}{1 + (\omega\tau_i)^{2a_i} + 2(\omega\tau_i)^{a_i}\cos\frac{\pi a_i}{2}}, \tag{13}$$

for the loss modulus as described by Costa and Ribeiro [25]. When $\alpha_i$ is set to one, the conventional GMM can be obtained. Owing to the extension of the equations, $1 + 3N$ parameters, namely $C_0$, $c_i$, $\tau_i$ and $\alpha_i$, must be determined. Further details on fractional calculus are omitted for brevity but can be found amongst others in Mainardi [26]. A complete set of material parameters corresponding to both models (GMM and GFMM) can be found in Tables 5–7 in the appendix.

### 2.3. Homogenisation of frequency dependent material behaviour

The discrete modelling of fibres and matrix with their different mechanical properties results in inhomogeneous states of stress and strain within the periodically deforming SRVE. In order to describe the macroscopic homogeneous material behaviour, averaged quantities are needed. The quantities obtained from an SRVE are homogenised by using a volume averaging scheme for averaged strains

$$\bar{\varepsilon}^*_{ij} = \frac{1}{V}\int_V \varepsilon^*_{ij}(x, y, z)\mathrm{d}V \tag{14}$$

and averaged stresses

$$\bar{\sigma}^*_{ij} = \frac{1}{V}\int_V \sigma^*_{ij}(x, y, z)\mathrm{d}V \tag{15}$$

at 50 discrete frequencies in the given range. Here, $V$ is the SRVE's volume. This averaging scheme ensures an equivalence in strain energy between the heterogeneous material and the homogenised macroscopic material characterised by the averaged strain and stress components. A mathematical demonstration of this equivalence is described by Sun and Vaidya [27].

At each frequency the complex stiffness tensor components are then calculated by the complex stress strain ratio as written down in Table 3 for all load cases and according to the correspondence principle. The resulting complex tensor components can be divided into real $\Re(\bar{C}^*_{ijkl})$ and imaginary $\Im(\bar{C}^*_{ijkl})$ parts representing storage $\bar{C}'_{ijkl}$ and loss $\bar{C}''_{ijkl}$ moduli, respectively.

These discrete values are now used to calibrate the above mentioned material models GMM and GFMM to represent the material at hand. In order to do so, the following error function

$$e = \xi_1 \frac{\sqrt{(\boldsymbol{y}'_{\mathrm{model}} - \boldsymbol{y}'_{\mathrm{exp}})^2}}{\sqrt{\boldsymbol{y}'^{\,2}_{\mathrm{exp}}}} + \xi_2 \frac{\sqrt{(\boldsymbol{y}''_{\mathrm{model}} - \boldsymbol{y}''_{\mathrm{exp}})^2}}{\sqrt{\boldsymbol{y}''^{\,2}_{\mathrm{exp}}}}, \tag{16}$$

is defined for both approaches to minimise the deviation between the model and the basic dataset [28].

Here, $\boldsymbol{y}'_{\mathrm{model}}$, $\boldsymbol{y}''_{\mathrm{model}}$ and $\boldsymbol{y}'_{\mathrm{exp}}$, $\boldsymbol{y}''_{\mathrm{exp}}$ are vectors containing model predictions and SRVE results at discrete circular frequencies ω, respectively. In addition, two weighting factors $\xi_1$ and $\xi_2$ are included. The minimisation is achieved by applying a global differential evolution algorithm and a local optimisation of global minimum by using a limited-Broyden–Fletcher–Goldfarb–Shanno-bound constraints (L-BFGS-B) algorithm.

**Table 3**
Determination of complex stiffness tensor components for all applied load cases.

| Load case | Determination of complex stiffness tensor entry | | |
|---|---|---|---|
| 1 | $\bar{C}^*_{1111}$ | $= \bar{\sigma}^*_{11}/\bar{\varepsilon}^*_{11}$ | $= \Re(\bar{C}^*_{1111}) + \mathrm{i}\Im(\bar{C}^*_{1111})$ |
| 2 | $\bar{C}^*_{2222}$ | $= \bar{\sigma}^*_{22}/\bar{\varepsilon}^*_{22}$ | $= \Re(\bar{C}^*_{2222}) + \mathrm{i}\Im(\bar{C}^*_{2222})$ |
| 3 | $\bar{C}^*_{1122}$ | $= \bar{\sigma}^*_{11}/\bar{\varepsilon}^*_{33}$ | $= \Re(\bar{C}^*_{1122}) + \mathrm{i}\Im(\bar{C}^*_{1122})$ |
| 4 | $\bar{C}^*_{1212}$ | $= \bar{\sigma}^*_{12}/\bar{\gamma}^*_{12}$ | $= \Re(\bar{C}^*_{1212}) + \mathrm{i}\Im(\bar{C}^*_{1212})$ |
| 5 | $\bar{C}^*_{1313}$ | $= \bar{C}^*_{1212}$ | $= \Re(\bar{C}^*_{1212}) + \mathrm{i}\Im(\bar{C}^*_{1212})$ |
| 6 | $\bar{C}^*_{2233}$ | $= \bar{C}^*_{2222} - 2\bar{\sigma}^*_{23}/\bar{\gamma}^*_{23}$ | $= \Re(\bar{C}^*_{2233}) + \mathrm{i}\Im(\bar{C}^*_{2233})$ |

**Table 4**
Coupon specimen dimensions and dynamic mechanical analysis test parameters.

| Lay-up | Length $l$/mm | Width $w$/mm | Thickness $t$/mm | Gauge length $l_0$ /mm | Displacement $\bar{u} \pm u_a$ /mm |
|---|---|---|---|---|---|
| $[0°]_8$ | 170 | 8 | 1.3 | 75 | 0.08 ± 0.0300 |
| $[\pm 45°]_{s2}$ | 170 | 8 | 1.3 | 75 | 0.08 ± 0.0300 |
| $[90°]_8$ | 167 | 25 | 1.3 | 72 | 0.15 ± 0.0288 |

## 3. Experimental validation tests

### 3.1. Manufacturing process and coupon specimen preparation

For the experimental validation test, common carbon-fibre-reinforced plastics (CFRP) prepreg material HexPly® M77/38%/UD150/CHS-12 K-T700 from Hexcel Corporation is used. Eight layers are laid-up by hand and cured in a hot moulding process at a temperature of 150°C by applying a pressure of 40 bar as recommended by the manufacturer. After the manufacturing process, coupon specimens are cut out by water jet cutting technology with the dimensions listed in Table 4.

### 3.2. Dynamic mechanical analysis

Dynamic mechanical analysis (DMA) tests are carried out according to ISO 6721-4 [29] on an Instron ElectroPuls E3000 testing machine equipped with a climate chamber in tension mode to gain temperature and frequency-dependent data of storage and loss modulus. The gauge length and the applied displacement values depend on the lay-up and are set to the values listed in Table 4. For all lay-ups, three coupon specimens are tested to obtain high accuracy in the measurement data.

All tests are displacement-controlled in a temperature range of − 60°C to 200°C (temperature increment: 2. 5°C) at the following frequencies: 0.1 Hz, 0.18 Hz, 0.32 Hz, 0.56 Hz, 1.0 Hz, 1.78 Hz, 3.0 Hz, 5.62 Hz and 10 Hz. The stiffness of the test setup is measured and taken into account with a correction factor. The elongation is then calculated from the crosshead displacement. The selected different loads are due to testing machine requirements and material properties. To determine the master curve for storage and loss modulus, the time-temperature superposition (TTS) is applied at a chosen reference temperature ($T_{\mathrm{ref}}$ = 135°C) according to Refs. [30,31]

$$\log_{10}(a_T) = \frac{-A(T - T_{\mathrm{ref}})}{B + (T - T_{\mathrm{ref}})}. \tag{17}$$

The coefficients $A$ and $B$ are determined by curve fitting when horizontal shift factors $a_T$ are plotted versus the temperature. Well-chosen coefficients ($A$ and $B$) lead to smooth master curves of storage and loss modulus. Both curves can be described over a wide frequency range and can be shifted to almost every reference temperature of interest.

## 4. Results

### 4.1. Influence of fibre volume content on the homogenised complex stiffness

Fig. 3 shows the storage $C'_{ijkl}$ and loss $C''_{ijkl}$ moduli for circular frequencies between $10^{-5}$ Hz to $10^6$ Hz after homogenisation of the results obtained from the SRVE simulations described above. In Fig. 3a), a significant dependency of the storage $C'_{1111}$ and loss $C''_{1111}$ modulus on the fibre volume content is noticeable. The highest value of the storage modulus $C'_{1111}$ = 161 GPa is reached for a fibre volume content of $v_f$ = 69 %, while the composite with the lowest fibre volume content $v_f$ = 30 % only reaches 75 GPa at high frequencies. Curves of the storage and loss modulus with fibre volume contents between $v_f$ = 30 % and $v_f$ = 69 % lie in between, where a higher fibre volume content leads to

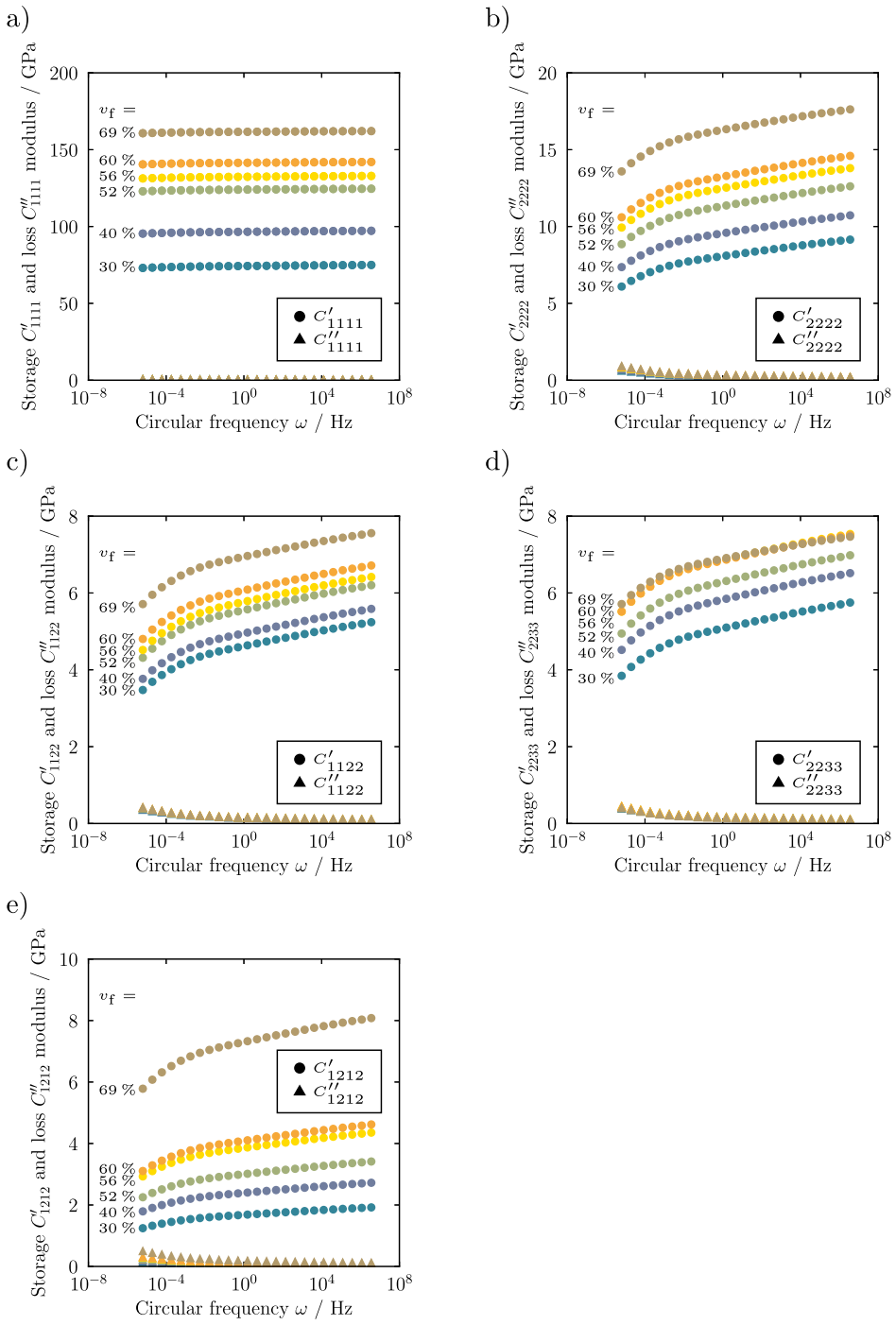


**Fig. 3.** Influence of fibre volume content $v_f$ in the SRVE on the homogenised storage and loss modulus of the complex modulus a) $C^*_{1111}$, b) $C^*_{2222}$, c) $C^*_{1122}$, d) $C^*_{2233}$ and e) $C^*_{1212}$ at temperature $T$ = 20°C.

an increase of storage modulus. Owing to the fibre orientation and the high Young's modulus of the fibres in contrast to the matrix, all storage $C'_{1111}$ and loss $C''_{1111}$ moduli show low circular frequency dependency.

The storage moduli $C'_{2222}$, $C'_{1122}$, $C'_{2233}$ and $C'_{1212}$ shown in Fig. 3b)–e) display a degressive increase over the circular frequency range. In contrast to that, the loss moduli $C''_{2222}$, $C''_{1122}$, $C''_{2233}$ and $C''_{1212}$ regressively decrease over the circular frequency.

### 4.2. Comparison of macroscopic material models

In the following the homogenised SRVE, the GMM and the GFMM are compared to each other for a fibre volume content of $v_f$ = 52% corresponding to the experimental findings. Based on common recommendations [24], the order $N^{GMM}$ = 11 is chosen corresponding to the number of decades under consideration. For the GFMM an order of $N^{GFMM}$ = 3 is specified based on a convergence study regarding the value of the error function $e$ in Eq. (16). For all of the aforementioned five complex stiffness tensor components the storage $C'$ and loss $C''$ moduli are determined over a circular frequency range of $10^{-6}$ Hz to $10^{6}$ Hz. However, only the components of the complex modulus $C^*_{1111}$ and $C^*_{2222}$ are shown representatively in Fig. 4. In general, the viscoelastic material behaviour can be described by both macroscopic material models, GMM and GFMM, with high accuracy compared to the homogenised SRVE results. Differences can be found in the number of

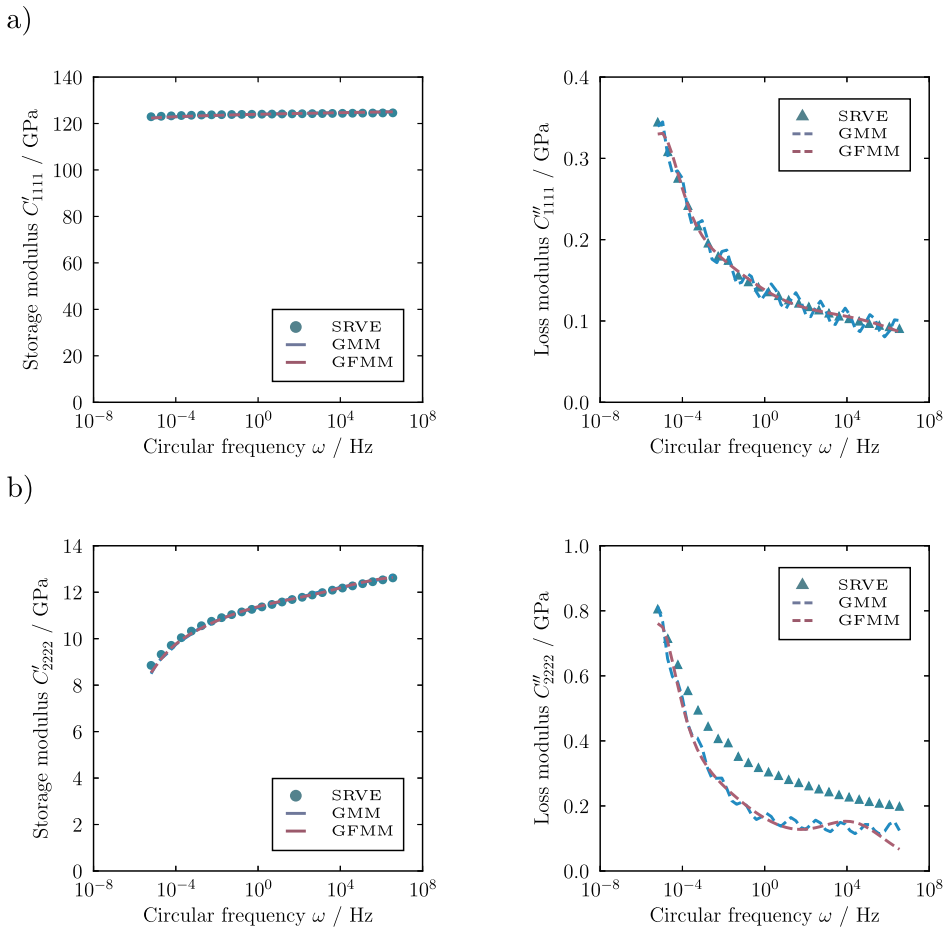


**Fig. 4.** a) Storage $C'_{1111}$ and loss $C''_{1111}$ modulus and b) storage $C'_{2222}$ and loss $C''_{2222}$ modulus for a fibre volume content $v_f = 52\%$ at temperature $T = 20°C$.

parameters ($N^{GMM} = 11$ and $N^{GFMM} = 3$) and in oscillation characteristics of GMM, owing to the mathematical description of the approaches.

Based on the error function in Eq. (16) the weighting $\xi_1$ and $\xi_2$ between storage and loss modulus is an essential factor. For this study, the weighting is on the storage modulus in order to accurately represent the vibration behaviour as shown in Fig. 4a). This in turn leads to an underestimated loss modulus for both approaches, GMM and GFMM, as it is illustrated in Fig. 4b). A smoother fit for storage and loss modulus can be achieved by applying GFMM as opposed to GMM where a typical oscillation can be observed. Overall, 23 parameters for GMM (corresponding to eleven Maxwell elements) and ten parameters for GFMM (corresponding to three factional Maxwell elements) must be determined to capture the desired circular frequency range for each storage and loss modulus. Furthermore, to reach the defined error $e = 0.3$ a number of 1050339 and 188222 function evaluations must be carried out leading to correspondingly long computing times for GMM in contrast to GFMM approach.

### 4.3. Validation of numerical results

A comparison of master curves between DMA measurements at room temperature $T = 20°C$ and those obtained from SRVE simulations is shown in Fig. 5. The complex moduli $E^*_L$, $E^*_T$ and $G^*_{LT}$ calculated according to Eq. (5) to Eq. (9) are considered. In contrast to the experimental DMA measurements, the longitudinal storage $E'_L$ and loss $E''_L$ modulus based on SRVE calculations is almost constant in the given circular frequency range, as shown in Fig. 5a). With a decrease of the circular frequency $\omega \leq 10^{-3}$ Hz, the experimental storage modulus $E'_L$ begins to decrease while the loss modulus $E''_L$ increases. In Fig. 5b) the curves of the transverse storage $E'_T$ and loss $E''_T$ modulus are illustrated. Here, the experimental storage modulus $E'_T$ shows a degressive increase whereas the loss modulus $E''_T$ regressively decreases over the circular frequency range. The matrix dominated mechanical material behaviour, i.e. the transverse properties, can be well depicted by SRVE calculations. However, for low circular frequencies the determined storage modulus $E'_T$ is slightly overestimated at low and slightly underestimated at high circular frequencies. For loss modulus $E''_T$ the curve shape behaves vice versa. At last, Fig. 5c) captures the storage $G'_{LT}$ and loss $G''_{LT}$ shear modulus studied by using ± 45° coupon specimens. The same material behaviour is observed as described above for the Young's modulus $E_T$, where the curves of storage $G'_{LT}$ and loss $G''_{LT}$ modulus can be described very well qualitatively by the SRVE, but on a slightly lower level for low circular frequencies.

### 4.4. Application on macro-scale

The results of a use case for the UMATs determining the natural frequencies $\omega_n$ and the effective damping ratios $D = -2\Re(\lambda)/|\Im(\lambda)|$, where $\lambda$ is the corresponding eigenvalue, of a cantilever beam with a $[90°/0°]_s$ and $[\pm 45°]_s$ layup are shown in Fig. 6a) and Fig. 6b). Here, the test setup (the beam is clamped on one side and excited by a harmonic force on the opposite side) is in accordance to ISO 6721-3 where the free length, width and thickness of the specimen is 100 mm, 10 mm and 1 mm, respectively. The results of GMM and GFMM are compared to an undamped linear elastic material model for the first four modes. All models predict the same natural frequencies for each mode. It should be noted, that mode three in Fig. 6a) is a torsional mode in contrast to the remainder being bending modes. In general, $[\pm 45°]_s$ laminates show higher effective damping ratios when bending modes are excited

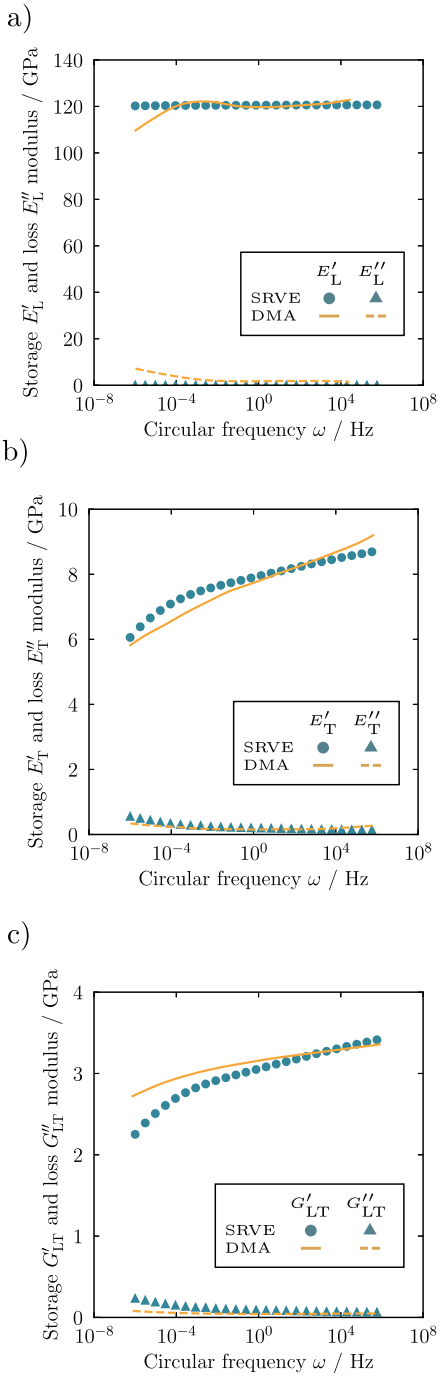


**Fig. 5.** a) Storage $E'_L$ and loss $E''_L$ modulus, b) storage $E'_T$ and loss $E''_T$ modulus and c) storage $G'_{LT}$ and loss $G''_{LT}$ modulus from experimental and numerical investigations for a fibre volume content $v_f = 52\%$ at temperature $T = 20°C$.

highlighting the anisotropic damping behaviour of the composite. The discrepancy of GMM and GFMM regarding the effective damping ratio can be attributed to the differing loss modulus as shown in Fig. 4.

## 5. Discussion

### 5.1. Influence of fibre volume content

The results of homogenising SRVEs with different fibre volume contents show that all stiffness tensor components exhibit the typical curves over the circular frequency range for their real and imaginary parts. For all effective storage components $\bar{C}_{ijkl}$ a higher fibre volume

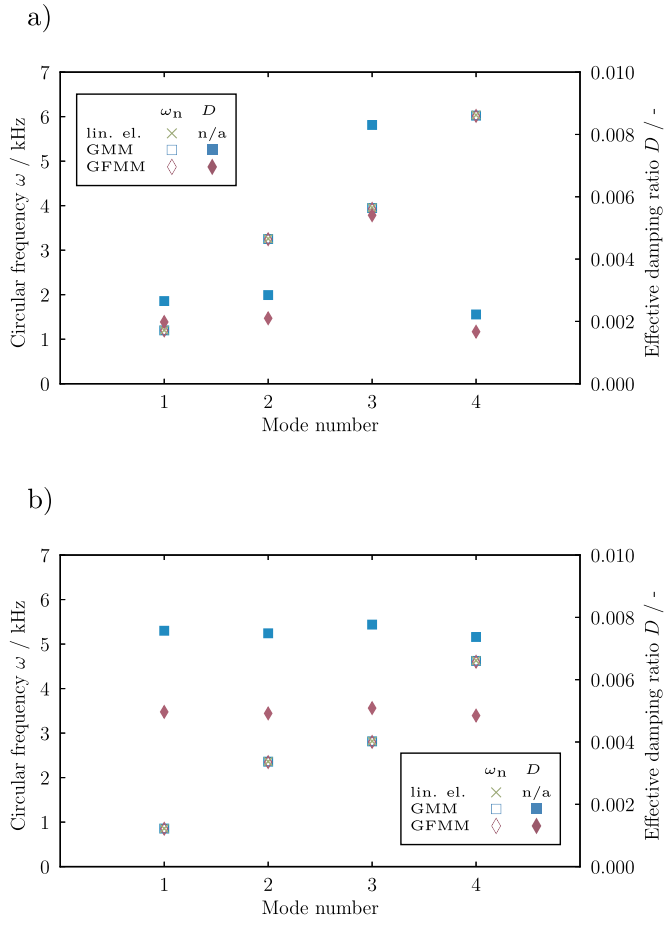


**Fig. 6.** Use case of a) $[90°/0°]_s$ and b) $[\pm 45°]_s$ cross-ply laminate cantilever beam by using user-defined material models under harmonic excitation.

content leads to a higher modulus underlining the reinforcement capabilities of the fibres. This relation is illustrated in Fig. 7, where the effective moduli $\bar{C}_{ijkl}$ and $\bar{C}_{ijkl}$ are normalised with regard to their respective value for a fibre volume content of $v_f = 30\%$ at a frequency of $f = 5$ Hz. It can be noted, that only the real component $\bar{C}_{1111}$ shows a linear increase. A similar behaviour is noted for the imaginary part $\bar{C}_{1111}$ where the component exhibits a linear decrease. Owing to the increasing fibre volume content, the shear properties of the fibres dominate the mechanical behaviour of the composite, leading to a significant increase of the complex modulus $\bar{C}^*_{1212}$. Hence, the fibre properties should be determined in detail or a methodology is to be developed in order to deduce the mechanical properties of the fibres by using reverse engineering of composites containing a high fibre volume content. The linear relations for both storage and loss moduli of the complex modulus $\bar{C}^*_{1111}$ suggest, that rules of mixture can be used to predict the viscoelastic material behaviour of an arbitrary composite based on data from different fibre volume contents. The limitations of applying rules of mixture to viscoelastic composites are discussed by Brinson and Knauss [3].

### 5.2. Comparison of macroscopic material models

The results of fitting the data obtained on the micro-scale to a macroscopic representation of the UD lamina show that the storage moduli are accurately depicted by the GMM/GFMM whereas the loss moduli of the material under investigation are underestimated by the GMM/GFMM in this work, i.e. the analytical equation of the GMM/GFMM is not able to capture the courses of both storage and loss modulus sufficiently for the given matrix. Therefore, the parameter

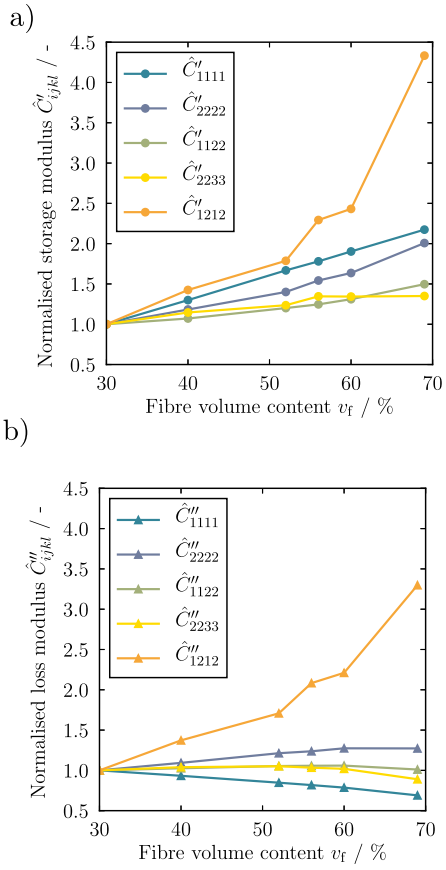


**Fig. 7.** Influence of fibre volume content $v_f$ on complex stiffness tensor components at $f = 5$ Hz.

identification procedure focuses on predicting the storage modulus accurately, which results in discrepancies in the loss modulus. The lack of experimental data of the master curve for the epoxy matrix and the corresponding insufficient assumption of the matrix material model in the SRVE might be a reason for this circumstance. Oscillations of the GMM approach are observed for the loss moduli and can only be minimised by increasing the number of parameters. The benefit of GFMMs in the elimination of oscillations while at the same time including fewer fit parameters is also observed by Costa et al. [32], Jóźwiak et al. [33] and Carrera et al. [34].

### 5.3. Validation of numerical results

The comparison of master curves obtained by means of SRVE simulations with those from DMA experiments show good agreement for the complex Young's modulus $E^*_L$. The high storage modulus compared to the low loss modulus, in both experimental and numerical results, clearly confirms that the mechanical behaviour in fibre direction is fibre dominated. The slight overestimation for low circular frequencies for SRVE in comparison with DMA data indicate, that the SRVE does not capture the loading conditions from the DMA experiment. While for the SRVE simulations an optimal load application onto the fibres is achieved by prescribing a homogeneous periodical deformation state, the experimental setup imposes the load on the matrix at first via the clamping. Upon consideration of the fact that DMA experiments are conducted at higher temperatures at which the epoxy matrix can be expected to soften significantly, it is assumed that the transfer of loads into the fibres is limited. Therefore, behaviour in fibre direction is more matrix dominated than it is in the simulations resulting in the observed higher dependency of the storage Young's modulus $E'_L$ on the circular frequency. The higher loss modulus observed in the experiment compared to the SRVE supports this explanation. Deviations in the master curves of $E'_T$, $E''_T$, $G'_{LT}$ and $G''_{LT}$, seen in Fig. 5, can be explained with incorrectly determined master curves for the epoxy matrix owing to the aforementioned lack of experimental data (see also Sec. 2.1), especially since the shift factors in the TTS equation do not only influence the horizontal position of the curves on the frequency scale but also the curves' shape. Therefore, a full experimental characterisation of the epoxy matrix by means of DMA in order to identify the shift factors for the neat matrix material is mandatory when good agreement with simulations is to be achieved. Furthermore, improved results could be obtained by taking into account relaxation as well as creep data in addition to the frequency-dependent data used here. This approach has previously been proven suitable by Sasso et al. [35] for parametrising viscoelastic material models based on experimentally determined data.

## 6. Conclusion

Within the scope of this work micro-scale simulations performed on SRVEs under periodic boundary conditions are used to identify master curves of five independent homogenised complex stiffness tensor components in the frequency domain. These five master curves fully describe the linear viscoelastic mechanical behaviour of the UD reinforced composite in the considered frequency range. Time and resource consuming time-domain simulations and, moreover, the conversion of the data obtained are thus avoided. Studies on the influence of the composite's fibre volume content show, that while the real part of all complex stiffness tensor components increases with higher fibre volume contents, where the component $\bar{C}_{1212}$ displays the highest influence. Similarly, the loss modulus $\bar{C}_{1212}$ increases significantly with increasing fibre volume content. Both can be drawn back to the discrepancy of the mechanical shear properties between fibre and matrix. For high fibre volume contents the mechanical fibre properties dominate the material behaviour of the composite. A comparison on the micro-scale obtained master curves with experimental DMA data of the same material yields small deviations with regard to Young's modulus in fibre direction. These deviations are attributed to the differences in load application in experiment and simulation. The Young's modulus in transverse direction deviates from the experiment with regard to the shape of storage and loss modulus curves, resulting from inaccuracies in modelling the viscoelastic matrix owing to incomplete experimental material characterisation. A full characterisation of the epoxy matrix via DMA is therefore considered essential in order to accurately model CFRP with the chosen approach in the frequency domain.

On the macro-scale, the obtained master curves are depicted by a generalised Maxwell model (GMM) and a generalised fractional Maxwell model (GFMM). The transversely isotropic UD lamina is represented by five independent components of the complex stiffness tensor. While the storage moduli are depicted well by both GMM and GFMM approach identified in this work, the loss moduli show deviations at high circular frequencies. Oscillations are characteristic of GMMs and can be avoided by using GFMMs. Both material models are implemented as user-defined material models for Abaqus and calibrated by using the parameters identified by homogenisation of SRVE results.

Future work on this subject could include the transition of the proposed material models into the time-domain while still using the same set of material parameters identified in the frequency domain. A study on the accuracy compared to material parameters identified in creep or relaxation tests in time-domain simulations should be conducted. Furthermore, the approach by Sasso et al. [35] mentioned above could be used to combine the numerically determined data from both domains in order to minimise the deviations seen between the predictions of the SRVEs and the parametrised models GMM and GFMM. Additionally nonlinear viscoelastic material models of the Schapery type could be parametrised by the frequency domain approach introduced in this work in order to better capture the behaviour of the given matrix system.

## Acknowledgement

This work is funded by the Deutsche Forschungsgemeinschaft (DFG, German Research Foundation) SPP1897 “Calm, Smooth, Smart – Novel approaches for influencing vibrations by means of deliberately introduced dissipation”, project KA 4224/3-1 and WE 4273/16-1 “HyCEML – Hybrid CFRP/elastomer/metal laminates containing elastomeric interfaces for deliberate dissipation” (Karlsruhe Institute of Technology). The authors would like to thank Hexcel Corporation for providing the material data. In addition, the authors want to acknowledge Siegfried Galkin providing the basic data for the statistically representative volume elements.

## Appendix A. Supplementary data

Supplementary data to this article can be found online at https://doi.org/10.1016/j.compscitech.2019.04.019.

## Appendix

Table 5
Equilibrium elastic material parameters of CFRP.

| | $C^*_{1111}$ | $C^*_{2222}$ | $C^*_{1122}$ | $C^*_{2233}$ | $C^*_{1212}$ |
|---|---|---|---|---|---|
| $C_0$/MPa | 125109.87 | 12781.12 | 6281.46 | 7071.35 | 3461.32 |

Table 6
Viscoelastic material parameters for GMM representation of CFRP.

| $N$ | $C^*_{1111}$ | | $C^*_{2222}$ | | $C^*_{1122}$ | | $C^*_{2233}$ | | $C^*_{1212}$ | |
|---|---|---|---|---|---|---|---|---|---|---|
| | $c_i$/– | $\tau_i$/s | $c_i$/– | $\tau_i$/s | $c_i$/– | $\tau_i$/s | $c_i$/– | $\tau_i$/s | $c_i$/– | $\tau_i$/s |
| 1 | $3.14{\cdot}10^{-3}$ | $1.22{\cdot}10^{+4}$ | $2.12{\cdot}10^{-2}$ | $7.35{\cdot}10^{-1}$ | $1.98{\cdot}10^{-2}$ | $2.92{\cdot}10^{-3}$ | $2.09{\cdot}10^{-2}$ | $7.95{\cdot}10^{-1}$ | $1.24{\cdot}10^{-1}$ | $1.59{\cdot}10^{+5}$ |
| 2 | $2.30{\cdot}10^{-3}$ | $8.08{\cdot}10^{+1}$ | $3.24{\cdot}10^{-2}$ | $1.23{\cdot}10^{+2}$ | $2.39{\cdot}10^{-2}$ | $9.90{\cdot}10^{+0}$ | $2.12{\cdot}10^{-2}$ | $5.28{\cdot}10^{-7}$ | $2.25{\cdot}10^{-2}$ | $2.43{\cdot}10^{-3}$ |
| 3 | $4.98{\cdot}10^{-3}$ | $1.35{\cdot}10^{+5}$ | $1.89{\cdot}10^{-2}$ | $1.78{\cdot}10^{-4}$ | $2.05{\cdot}10^{-2}$ | $4.67{\cdot}10^{-2}$ | $5.87{\cdot}10^{-2}$ | $1.48{\cdot}10^{+4}$ | $6.43{\cdot}10^{-2}$ | $1.41{\cdot}10^{+4}$ |
| 4 | $1.91{\cdot}10^{-3}$ | $5.94{\cdot}10^{+0}$ | $5.94{\cdot}10^{-2}$ | $1.46{\cdot}10^{+4}$ | $1.87{\cdot}10^{-2}$ | $1.00{\cdot}10^{-5}$ | $3.19{\cdot}10^{-2}$ | $1.28{\cdot}10^{+2}$ | $4.71{\cdot}10^{-2}$ | $1.41{\cdot}10^{+3}$ |
| 5 | $1.67{\cdot}10^{-3}$ | $2.95{\cdot}10^{-2}$ | $1.16{\cdot}10^{-1}$ | $1.59{\cdot}10^{+5}$ | $1.17{\cdot}10^{-1}$ | $1.59{\cdot}10^{+5}$ | $1.98{\cdot}10^{-2}$ | $5.22{\cdot}10^{-2}$ | $2.56{\cdot}10^{-2}$ | $4.55{\cdot}10^{-7}$ |
| 6 | $1.57{\cdot}10^{-3}$ | $1.92{\cdot}10^{-3}$ | $2.36{\cdot}10^{-2}$ | $1.01{\cdot}10^{+1}$ | $2.15{\cdot}10^{-2}$ | $7.13{\cdot}10^{-1}$ | $1.84{\cdot}10^{-2}$ | $1.89{\cdot}10^{-4}$ | $2.61{\cdot}10^{-2}$ | $8.57{\cdot}10^{+0}$ |
| 7 | $1.48{\cdot}10^{-3}$ | $1.16{\cdot}10^{-4}$ | $1.94{\cdot}10^{-2}$ | $3.00{\cdot}10^{-3}$ | $1.93{\cdot}10^{-2}$ | $1.74{\cdot}10^{-4}$ | $1.90{\cdot}10^{-2}$ | $3.23{\cdot}10^{-3}$ | $2.30{\cdot}10^{-2}$ | $3.83{\cdot}10^{-2}$ |
| 8 | $1.40{\cdot}10^{-3}$ | $6.58{\cdot}10^{-6}$ | $2.02{\cdot}10^{-2}$ | $4.82{\cdot}10^{-2}$ | $2.22{\cdot}10^{-2}$ | $5.06{\cdot}10^{-7}$ | $2.33{\cdot}10^{-2}$ | $1.08{\cdot}10^{+1}$ | $2.13{\cdot}10^{-2}$ | $8.83{\cdot}10^{-6}$ |
| 9 | $2.57{\cdot}10^{-3}$ | $1.08{\cdot}10^{+3}$ | $4.30{\cdot}10^{-2}$ | $1.48{\cdot}10^{+3}$ | $6.01{\cdot}10^{-2}$ | $1.45{\cdot}10^{+4}$ | $1.14{\cdot}10^{-1}$ | $1.59{\cdot}10^{+5}$ | $2.37{\cdot}10^{-2}$ | $5.93{\cdot}10^{-1}$ |
| 10 | $1.50{\cdot}10^{-3}$ | $3.33{\cdot}10^{-7}$ | $1.84{\cdot}10^{-2}$ | $1.02{\cdot}10^{-5}$ | $4.36{\cdot}10^{-2}$ | $1.47{\cdot}10^{+3}$ | $1.79{\cdot}10^{-2}$ | $1.06{\cdot}10^{-5}$ | $3.56{\cdot}10^{-2}$ | $1.14{\cdot}10^{+2}$ |
| 11 | $1.78{\cdot}10^{-3}$ | $4.29{\cdot}10^{-1}$ | $2.19{\cdot}10^{-2}$ | $5.11{\cdot}10^{-7}$ | $3.28{\cdot}10^{-2}$ | $1.22{\cdot}10^{+2}$ | $4.24{\cdot}10^{-2}$ | $1.51{\cdot}10^{+3}$ | $2.20{\cdot}10^{-2}$ | $1.49{\cdot}10^{-4}$ |

Table 7
Viscoelastic material parameters for GFMM representation of CFRP.

| | $N$ | $c_i$/- | $\tau_i$/s | $\alpha_i$/- |
|---|---|---|---|---|
| $C^*_{1111}$ | 1 | $1.35{\cdot}10^{-2}$ | $2.93{\cdot}10^{-5}$ | $1.34{\cdot}10^{-1}$ |
| | 2 | $1.35{\cdot}10^{-2}$ | $1.57{\cdot}10^{+3}$ | $2.08{\cdot}10^{-1}$ |
| | 3 | $6.80{\cdot}10^{-3}$ | $1.59{\cdot}10^{+5}$ | $5.65{\cdot}10^{-1}$ |
| $C^*_{2222}$ | 1 | $3.01{\cdot}10^{-1}$ | $7.86{\cdot}10^{+3}$ | $1.91{\cdot}10^{-1}$ |
| | 2 | $6.70{\cdot}10^{-2}$ | $5.09{\cdot}10^{-5}$ | $3.52{\cdot}10^{-1}$ |
| | 3 | $1.43{\cdot}10^{-1}$ | $1.59{\cdot}10^{+5}$ | $6.29{\cdot}10^{-1}$ |
| $C^*_{1122}$ | 1 | $3.06{\cdot}10^{-1}$ | $8.67{\cdot}10^{+3}$ | $1.91{\cdot}10^{-1}$ |
| | 2 | $6.93{\cdot}10^{-2}$ | $5.45{\cdot}10^{-5}$ | $3.49{\cdot}10^{-1}$ |
| | 3 | $1.44{\cdot}10^{-1}$ | $1.59{\cdot}10^{+5}$ | $6.30{\cdot}10^{-1}$ |
| $C^*_{2233}$ | 1 | $6.42{\cdot}10^{-2}$ | $4.99{\cdot}10^{-5}$ | $3.56{\cdot}10^{-1}$ |
| | 2 | $2.94{\cdot}10^{-1}$ | $7.15{\cdot}10^{+3}$ | $1.92{\cdot}10^{-1}$ |
| | 3 | $1.43{\cdot}10^{-1}$ | $1.59{\cdot}10^{+5}$ | $6.29{\cdot}10^{-1}$ |
| $C^*_{1212}$ | 1 | $8.28{\cdot}10^{-2}$ | $6.06{\cdot}10^{-5}$ | $3.37{\cdot}10^{-1}$ |
| | 2 | $3.43{\cdot}10^{-1}$ | $1.20{\cdot}10^{+4}$ | $1.88{\cdot}10^{-1}$ |
| | 3 | $1.47{\cdot}10^{-1}$ | $1.59{\cdot}10^{+5}$ | $6.25{\cdot}10^{-1}$ |

## References

[1] R.A. Schapery, Stress analysis of viscoelastic composite materials, J. Compos. Mater. 1 (3) (1967) 228–267.
[2] C. Hiel, A.H. Cardon, H.F. Brinson, The Nonlinear Viscoelastic Response of Resin Matrix Composite Laminates, Tech. Rep. NASA CR-3772 National Aeronautics and Space Administration, Washington, D. C., July 1984.
[3] L.C. Brinson, W.G. Knauss, Finite element analysis of multiphase viscoelastic solids, J. Appl. Mech. 59 (4) (1992) 730–737.
[4] S.W. Park, R.A. Schapery, Methods of interconversion between linear viscoelastic material functions. Part I – a numerical method based on Prony series, Int. J. Solids

Struct. 36 (11) (1999) 1653–1675.
[5] R.A. Schapery, S.W. Park, Methods of interconversion between linear viscoelastic material functions. Part II – an approximate analytical method, Int. J. Solids Struct. 36 (11) (1999) 1677–1699.
[6] G. de Prony, Essai expérimental et analytique sur les lois de la dilatabilité des fluides élastiques et sur celles de la force expansive de la vapeur de l'eau et de la vapeur de l'alcool à différentes températures, J. l'École Polytech. Floréal Plairial 1 (22) (1795) 24–76.
[7] M. Kaliske, H. Rothert, Formulation and implementation of three-dimensional viscoelasticity at small and finite strains, Comput. Mech. 19 (3) (1997) 228–239.
[8] A. Naik, N. Abolfathi, G. Karami, M. Ziejewski, Micromechanical viscoelastic characterization of fibrous composites, J. Compos. Mater. 42 (12) (2008) 1179–1204.
[9] A. Rösner, L. Kärger, F. Henning, Virtual characterization and macroscopic material modeling of a carbon fiber-reinforced PA6 UD composite, J. Compos. Mater. 51 (21) (2017) 3075–3086.
[10] V.G. Martynenko, G.I. Lvov, Numerical prediction of temperature-dependent anisotropic viscoelastic properties of fiber reinforced composite, J. Reinf. Plast. Compos. 36 (24) (2017) 1790–1801.
[11] R. Ansari, M.K. Hassazadeh-Aghdam, Micromechanical investigation of creep-recovery behavior of carbon nanotube-reinforced polymer nanocomposites, Int. J. Mech. Sci. 115–116 (2016) 45–55.
[12] M.K. Hassazadeh-Aghdam, R. Ansari, M.J. Mahmoodi, A. Darvizeh, Effect of nanoparticle aggregation on the creep behavior of polymer nanocomposites, Compos. Sci. Technol. 162 (2018) 93–100.
[13] M.V. Pathan, V.L. Tagarielli, S. Patsias, Numerical predictions of the anisotropic viscoelastic response of uni-directional fibre composites, Compos. Part A 93 (2017) 18–32.
[14] M.V. Pathan, S. Patsias, J.A. Rongong, V.L. Tagarielli, Measurements and predictions of the viscoelastic properties of a composite lamina and their sensitivity to temperature and frequency, Compos. Sci. Technol. 149 (2017) 207–219.
[15] S. Javid, G. Karami, F. Azarmi, Micromechanics of unidirectional viscoelastic fibrous composites-homogenized vs local characterization, J. Multifunct. Compos. 1 (1) (2013) 35–48.
[16] M. El Hachemi, Y. Koutsawa, H. Nasser, G. Giunta, A. Daouadji, E.M. Daya, S. Belouettar, An intuitive computational multi-scale methodology and tool for the dynamic modelling of viscoelastic composites and structures, Compos. Struct. 144 (2016) 131–137.
[17] A. Melro, P. Camanho, S. Pinho, Generation of random distribution of fibres in long-fibre reinforced composites, Compos. Sci. Technol. 68 (9) (2008) 2092–2102.
[18] A. Melro, P. Camanho, F.M. Andrade Pires, S. Pinho, Numerical simulation of the non-linear deformation of 5-harness satin weaves, Comput. Mater. Sci. 61 (2012) 116–126.
[19] Toray Carbon Fibers America, Inc., Technical data sheet No. CFA-005, (November 2002).
[20] H. Schürmann, Konstruieren mit Faser-Kunststoff-Verbunden, Springer, 2005.
[21] Hexcel Corporation, Product Data Sheet HexPly® M77, (March 2014).
[22] W.T. Read, Stress analysis for compressible viscoelastic materials, J. Appl. Phys. 21 (7) (1950) 671–674.
[23] P. Haupt, Continuum Mechanics and Theory of Materials, Springer, 2002.
[24] Dassault Systemes, Abaqus Documentation, (2017).
[25] M.F.P. Costa, C. Ribeiro, Generalized fractional maywell model: parameter estimation of a viscoelastic material, AIP Conference Proceedings, vol. 1479, 2012, pp. 790–793.
[26] F. Mainardi, Fractional Calculus and Waves in Linear Viscoelasticity, Imperial College Press, 2010.
[27] C.T. Sun, R.S. Vaidya, Prediction of composite properties from a representative volume element, Compos. Sci. Technol. 56 (2) (1996) 171–179.
[28] J. Bergström, Mechanics of Solid Polymers: Theory and Computational Modeling, Elsevier, 2015.
[29] International Organization for Standardization, Plastics - Determination of Dynamic Mechanical Properties - Part 4: Tensile Vibration - Non-resonance Method, ISO 6721-4, May 2008.
[30] M.L. Williams, R.F. Landel, J.D. Ferry, The temperature dependence of relaxation mechanisms in amorphous polymers and other glass-forming liquids, J. Am. Chem. Soc. 77 (14) (1955) 3701–3707.
[31] J.D. Ferry, Viscoelastic Properties of Polymers, John Wiley & Sons, Inc., 1980.
[32] M.F.P. Costa, C. Ribeiro, Parameter estimation of viscoelastic materials: a test case with different optimization strategies, AIP Conference Proceedings, vol. 1389, 2011, pp. 771–774.
[33] B. Jóźwiak, M. Orczykowska, M. Dziubiński, Fractional generalizations of Maxwell and Kelvin-Voigt models for biopolymer characterization, PLoS One 10 (11) (2015) 1–19.
[34] Y. Carrera, G. Avila-de la Rosa, E.J. Vernon-Carter, J. Alvarez-Ramirez, A fractional-order Maxwell model for non-Newtonian fluids, J. Appl. Mech. 482 (2017) 276–285.
[35] M. Sasso, G. Palmieri, D. Amodio, Application of fractional derivative models in linear viscoelastic problems, Mech. Time-Dependent Mater. 15 (4) (2011) 367–387.